Dynamically tunable hydrodynamic transport in boron nitride-encapsulated graphene

Akash Gugnani, ^{1,*} Aniket Majumdar, ^{1,†} Kenji Watanabe, ² Takashi Taniguchi, ³ and Arindam Ghosh^{1,4,‡}

¹ Department of Physics, Indian Institute of Science, Bangalore 560012, India

² Research Center for Electronic and Optical Materials,

National Institute for Materials Science, 1-1 Namiki, Tsukuba 305-0044, Japan

³ Research Center for Materials Nanoarchitectonics,

National Institute for Materials Science, 1-1 Namiki, Tsukuba 305-0044, Japan

⁴ Center for Nano Science and Engineering, Indian Institute of Science, Bangalore 560012, India

Over the past decade, graphene has emerged as a promising candidate for exploring the viscous nature of electronic flow facilitated by the availability of extremely high-quality devices employing a graphene channel encapsulated within dielectric layers of hexagonal boron nitride (hBN). However, the level of disorder in such systems is mainly determined by the device fabrication protocols, making it impossible to obtain a tunability between the impurity-dominated and the viscous transport within the same device. In this work, using a combination of ultraviolet (UV) radiation and gate electric field, we have demonstrated a dynamic modulation of charge hydrodynamics, quantified in the thermal and electrical transport by the extent of departure from the Wiedemann-Franz (WF) Law in monolayer graphene devices at room temperature. We achieved this by tuning the disorder level continuously and reversibly using UV light to create transient trap states in the encapsulating hBN dielectric. With progressive UV radiation, we observed a dramatic increase in the momentum-relaxing scattering relative to that between the electrons and also the Lorentz number, by nearly a factor of ten, with increasing disorder, thereby approaching the restoration of the WF law in highly disordered graphene. Our experiments outline a potent strategy to tune the fundamental mechanism of charge flow in state-of-the-art graphene devices.

INTRODUCTION

The hydrodynamic flow of electrons in mesoscopic systems has garnered significant attention in the past decade, owing to the emergence of ultra-clean twodimensional materials like graphene [1, 2], transition metal dichalcogenides [3, 4], etc. The fluidic motion of electrons, characterised by strong momentum-conserving electron-electron interactions, has been detected experimentally through the observation of Planckian scattering [5], parabolic velocity profile [6–8], negative local resistance [9], giant thermal diffusivity [10], Hall viscosity [11, 12], WF law violation [13], electron vortices [14], universal viscosity-to-entropy density lower bound [15], etc. A common principle advocated by these experiments for realising electron hydrodynamics is that the electron-electron scattering timescale (τ_{ee}) must be much shorter than any momentum-relaxing scattering process $(\tau_{\rm mr})$, like electron-impurity scattering, diffuse scattering from the boundary, electron-phonon scattering etc. However, recent experiments [16] have reported viscous electron flow even while violating the above criterion, opening up alternative routes towards electron hydrodynamics, such as para-hydrodynamics [17], retroreflected hole backflow [18], and tomographic electron transport [19, 20]. Therefore, it is imperative to study the interplay between momentum-conserving and momentum-relaxing collisions to understand and engineer the electron hydrodynamics in graphene.

Modern device fabrication techniques [21–23] have made it possible to significantly minimise the intrinsic disorder concentration and charge inhomogeneity (indicated by $n_{\min}(0)$ in exfoliated two-dimensional layers. For monolayer graphene, $n_{\min}(0)$ can go down to as low as 10^9 cm⁻² [24, 25] in state-of-the-art field effect transistor (FET) devices. However, existing graphene FETs suffer from a lack of tunability of the impurity concentration as the $n_{\min}(0)$ is solely determined by the fabrication protocols. Recent efforts to explore the controlled implantation of disorder in bad metals utilising helium ion irradiation [26] were successful, but they lead to permanent degradation of the sample, thereby impeding the demonstration of a reversible hydrodynamic-to-diffusive crossover. UV radiation, on the other hand, has been used as a tuning knob [27–29] to transfer charges across the different layers of graphene-hBN-based van der Waals (vdW) heterostructures. These transferred charges can operate as free carriers and contribute to the electrical current, or get trapped within the dielectric, causing fluctuations in the background potential, leading to the formation of charge inhomogeneity across the sample. Moreover, by applying a gate electric field [30, 31], one can control the number of carriers getting transferred as well as the direction of transfer, thereby creating a new avenue for achieving precisely reversible disorder-doping interplay of the electronic channel.

In this work, we have chosen high-quality monolayer graphene FETs encapsulated within multi-layered hBN flakes as the platform for realising electron hydrodynamics. Further, we have employed UV radiation as a tool to controllably modulate the extent of charge disorder subjected to the graphene layer and have explored the mechanisms of the electrical transport at room temperature. Using noise thermometry, we have found that the

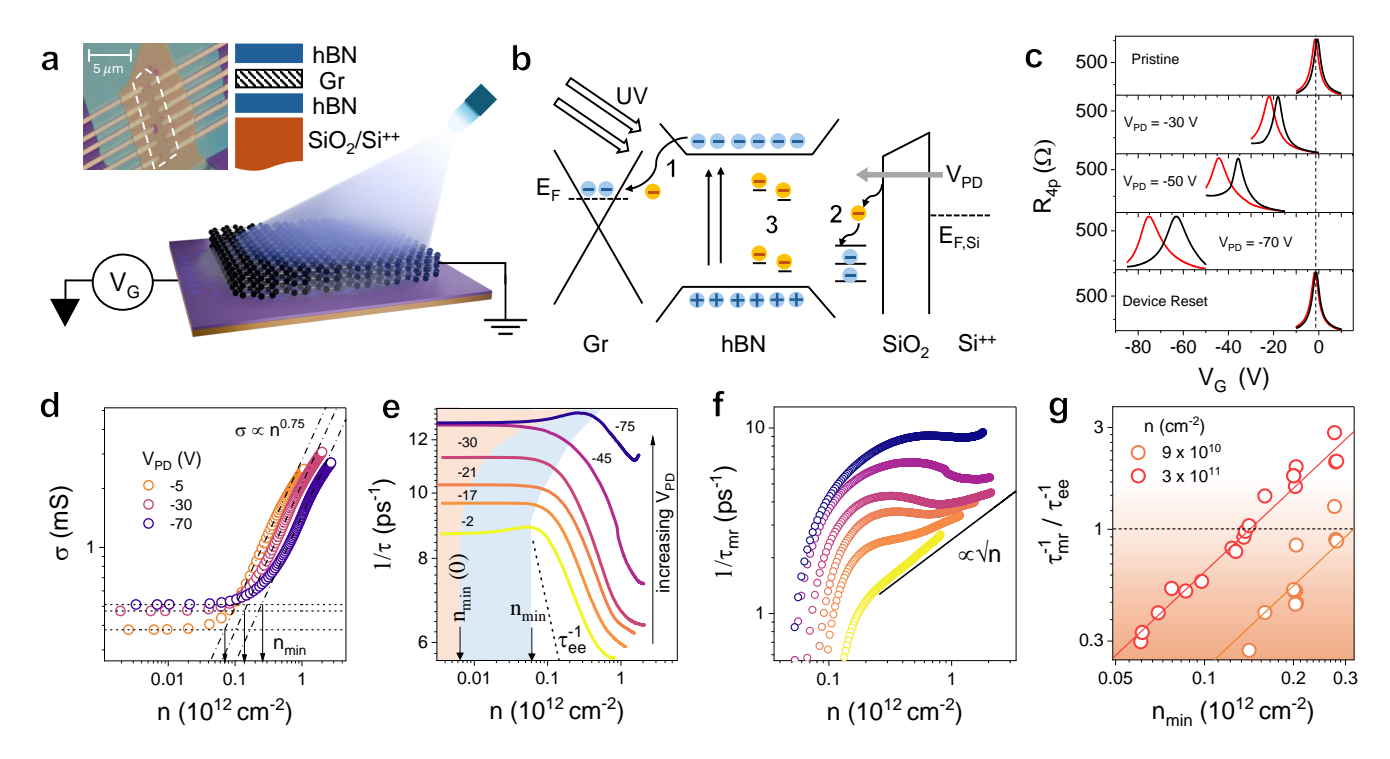


Figure 1. Tuning electronic disorder using UV radiation: (a). Top-left corner shows the optical micrograph of one of the measured devices (D3). The cross-sectional view of the heterostructure is shown to its right. [Below] Schematic of the experimental setup used for performing UV radiation-based tuning of disorder. (b) Different mechanisms responsible for charge redistribution upon UV illumination (indicated using thick white arrows with black border). Process 1 refers to UV-induced photographene or vice versa. Process 2 indicates the formation of charge puddles in the mid-gap states of hBN as a result of UV excitation. Process 3 marks the onset of UV-induced activation of trap states at the hBN-SiO₂ interface and subsequent random trapping of charges at those sites. The blue-coloured charges are intrinsic charges residing in the different layers, while the yellow-coloured ones are the UV radiation-induced charges which have been redistributed across the heterostructure. (c) Variation of four-terminal resistance R_{4p} as a function of gate voltage $V_{\rm G}$ for both forward and backward $V_{\rm G}$ sweeps at four different values of $V_{\rm PD}$. The panel at the bottom shows the characteristics obtained by resetting the device to pristine condition (indicated by a vertical dotted line) by shining UV radiation at $V_{\rm PD}=0~{
m V}$. (d) Variation of electrical conductivity (σ) with n in device D3 for different values of $V_{\rm PD}$. The resulting $n_{\rm min}$ for each of these traces has been obtained by noting the intersection between the lines $\sigma = \sigma_{\rm min}$ (dotted line) and $\sigma \propto n^{0.75}$ (dashed line), where σ_{\min} is the electrical conductivity at the Dirac point. (e) Variation of the total scattering rate τ^{-1} as a function of n for different values of $V_{\rm PD}$. The dashed line shows the variation of electron-electron relaxation scattering rate $\tau_{\rm ee}^{-1}$ with n. The $n < n_{\min}(0)$ region is colored with light red, whereas $n_{\min}(0) \le n \le n_{\min}$ region is colored with light blue. (f) Variation of the momentum relaxation scattering rate $\tau_{\rm mr}^{-1}$ as a function of n for the same values of $V_{\rm PD}$, as those depicted in panel (e). The solid line indicates a \sqrt{n} dependence. (g) Ratio of momentum relaxation scattering rate $(\tau_{\rm mr}^{-1})$ to the electron-electron scattering rate $(\tau_{\rm ee}^{-1})$ as a function of $n_{\rm min}$ for two different carrier densities. The solid lines vary as $n_{\rm min}$ and serve as a guide to the eye. The colored region corresponding to $\tau_{\rm mr}^{-1}/\tau_{\rm ee}^{-1}<1$ indicates the viscous limit, while the region with $\tau_{\rm mr}^{-1}/\tau_{\rm ee}^{-1}>1$ indicates the diffusive limit.

introduction of disorder tends to restore the thermal conductivity to the classical Wiedemann-Franz (WF) [32] value, given by $\kappa_e = \mathcal{L}_{\text{WF}} \, \sigma T$ where κ_e is the electronic contribution to thermal conductivity, σ is the electrical conductivity and $\mathcal{L}_{\text{WF}} = \pi^2 k_{\text{B}}^2/3e^2$, with k_{B} and e being the Boltzmann constant and the electronic charge respectively. This technique allows one to reversibly tune a high-quality graphene device from the hydrodynamic regime into the diffusive regime and back, at a temperature as high as 300 K, providing crucial insights on the interplay of momentum-conserving and momentum-relaxing collisions in the emergence of viscous electronic flow.

ELECTRICAL CHARACTERISATION OF UV-IRRADIATED GRAPHENE LAYERS

Mechanically exfoliated graphene flakes, after encapsulation using hBN, were transferred onto a Si⁺⁺/SiO₂ substrate and etched into rectangles ($\simeq 20~\mu\mathrm{m} \times 10~\mu\mathrm{m}$), and electrical contact was established using edge-contacted gold electrodes (Fig. 1a, see also Supplementary Section S1). The total charge inhomogeneity present in these vdW heterostructures at temperature T is given by n_{\min} where $n_{\min} = n_{\min}(0) + n_{\mathrm{th}}(T)$, with $n_{\mathrm{th}}(T) = (2\pi^3/3)(k_{\mathrm{B}}T/hv_{\mathrm{F}})^2$ referring to the thermally excited carrier density at temperature T [15, 24, 33] (h, k_{B} and

 $v_{\rm F}$ are the Planck's constant, Boltzmann's constant and Fermi velocity respectively). The high quality of the devices can be attributed to the low intrinsic charge inhomogeneity values, quantified using the residual charge carrier density $n_{\rm min}(0) \simeq 7 \times 10^9 \ {\rm cm}^{-2}$. Additionally, the strain-induced gap in the density of states was estimated to be too small to impact our experiments, which were carried out at room temperature. (See Supplementary Section S2). To tune the background potential fluctuations, the graphene devices were subjected to a gate electric voltage (called the photo-doping voltage $V_{\rm PD}$) and uniformly irradiated using UV radiation (Fig. 1a) with wavelength $\lambda = 235$ nm and a constant power density $\approx 1 \text{ pW}/\mu\text{m}^2$ (Details in Supplementary Section S3). The consequent light-matter interaction within the encapsulating hBN layers results in the redistribution of charges within the vdW heterostructure via two different mechanisms (Fig. 1b) -

- (1) Interlayer charge transfer The band gap (E_g) of hBN is $\simeq 5$ eV [34]. Upon UV illumination $(hc/\lambda \gtrsim$ $E_{\rm g}$), electron-hole pairs are generated and the applied electric field prevents the recombination of photo-induced carriers, leading to a migration of electrons (holes) from hBN to graphene (indicated in Fig. 1b as Process-1), under the application of a negative (positive) $V_{\rm PD}$. This process is identical to photogating [30]; as a result, the Dirac point shifts close to $V_{\rm PD}$ for both forward and backwards gate voltage $(V_{\rm G})$ sweeps (See Supplementary Section S4-a). Upon applying a $V_{\rm PD}$ as large as -70 V to the Si substrate, the graphene channel undergoes photo-doping by nearly $3\times 10^{11}~\mathrm{cm^{-2}}$ - a process generating $\approx 10^9$ cm⁻² carriers per unit volt of $V_{\rm PD}$, which corresponds to a shift in Fermi energy $(E_{\rm F})$ by just 6.5 meV. (See Supplementary Section S4-b).
- (2) Random charge trapping UV radiation can also activate random shallow and deep trap states at the hBN-SiO₂ interface [35] (indicated in Fig. 1b as Process-2) alongside localised charge puddles within the hBN layer [36–38] (shown in Fig. 1b as Process-3), resulting in a decrease in carrier mobility (μ) of the channel (See Supplementary Section S4-c and S4-d) by almost an order of magnitude - from 2 m² V⁻¹ s⁻¹ to $0.3 \text{ m}^2 \text{ V}^{-1} \text{ s}^{-1}$ as V_{PD} is swept from 0 V to -70 V. Additionally, in both forward and backwards gate voltage sweeps, the transfer characteristics show an increasing anti-hysteresis and transform from a sharp to a broader Lorentzian peak, with increasing $V_{\rm PD}$ (Fig. 1c). This increase in full width at half maximum (FWHM) of the peak is directly proportional to the increasing total charge inhomogeneity (n_{\min}) , which has been evaluated from the x-intercept of the intersection between $\sigma = \sigma_{\min}$ and $\sigma \propto n^{\gamma}$ ($\gamma \simeq 1$), where σ_{\min} is the electrical conductivity at the Dirac point (Fig. 1d).

UV radiation can also lead to permanent degradation of the graphene layer [39]. However, we observe that the graphene channel with its CNP around -70 V (Fig. 1c), under UV illumination with $V_{\rm PD}=0$ V, experiences a

shift in Dirac point from $\approx -75~\mathrm{V}$ to $\approx -0.5~\mathrm{V}$ and the pristine electrical characteristics of the graphene FET are revived (Fig. 1c, bottom-most panel). This restoration of the disorder level to the pristine condition via UV-induced extrinsic hole doping (Details in Supplementary Section S5) confirms the reversible nature of disorder tunability of this technique.

The combined effect of the above-mentioned mechanisms leads to a competition between the momentum relaxation scattering rate $(\tau_{\rm mr}^{-1})$ of the electrons in the disordered graphene device and the momentum conserving electron-electron scattering rate (τ_{ee}^{-1}) , which is determined only by T when $T > T_{\rm F}$ (and $T_{\rm F}$ when $T_{\rm F} >$ T). $\tau_{\rm mr}^{-1}$ is obtained from the experimental quasiparticle relaxation rate τ^{-1} (Fig. 1e), which is given by $\tau = \sigma \hbar k_{\rm F}/v_{\rm F} n e^2$, with $n, \hbar, k_{\rm F}$ and e being the net carrier density measured relative to the instantaneous charge neutrality point (CNP), the reduced Planck's constant, Fermi wave vector and the electronic charge respectively. Applying Matthiessen's rule, in the leading order, we get $au^{-1} = au_{mr}^{-1} + au_{ee}^{-1}$ where au_{ee}^{-1} is the electron-electron scattering rate, which, in the presence of a finite Fermi surface, is given by $\tau_{\rm ee}^{-1} \approx (\alpha k_{\rm B} T/\hbar v_{\rm F})^2 (v_{\rm F}/k_{\rm F}) \ (\alpha \approx 0.5$ [40, 41] being the fine structure constant). The resulting τ_{mr}^{-1} is plotted in Fig. 1f as a function of n for the same set of $V_{\rm PD}$ used in Fig. 1e. In pristine graphene, momentum relaxation at high electron densities is driven by electron-acoustic phonon scattering [42, 43], and the scattering rate scales as

$$\tau_{\rm el-ph}^{-1} = \frac{1}{\hbar^2} \frac{E_{\rm F}}{4v_{\rm F}} \frac{D^2}{\rho_{\rm m} v_{\rm ph}^2} k_{\rm B} T \propto \sqrt{n}$$
(1)

where $\rho_{\rm m}$ is the mass density of graphene, $v_{\rm ph}$ is the acoustic phonon velocity, $E_{\rm F}$ is Fermi Energy, and D is the deformation potential [44]. The experimental data points, as indicated in Fig. 1f, agree well with Eqn. 1and the acoustic phonon deformation potential D is evaluated to be $\simeq 15$ eV, which agrees with previous experimental estimates [45, 46]. The addition of disorder to the channel provides one more pathway to relax the momentum - Coulomb force-mediated electronimpurity scattering [47–49], yielding $\tau_{\rm el-imp}^{-1} \propto \sqrt{n}$ (Details in Supplementary Section S6). Finally, the ratio of the momentum-relaxing and momentum-conserving scattering rates, denoted by $\tau_{\rm mr}^{-1}/\tau_{\rm ee}^{-1}$ in Fig. 1g, as a function of UV-induced disorder n_{\min} demonstrates the crossover of electrical transport in the graphene channel from the clean limit $(\tau_{\rm mr}^{-1}/\tau_{\rm ee}^{-1}<1)$ to the dirty limit $(\tau_{\rm mr}^{-1}/\tau_{\rm ee}^{-1}>1)$. We note that the critical disorder density required to achieve this crossover depends on the Fermi energy level of the graphene channel, with doped graphene $(n \simeq 10^{11} \text{ cm}^{-2})$ requiring lower amounts of disorder while undoped graphene ($n \approx 10^{10} \text{ cm}^{-2}$) experiencing momentum-conserved electronic scattering over the entire range of experimentally accessible disorder concentrations.

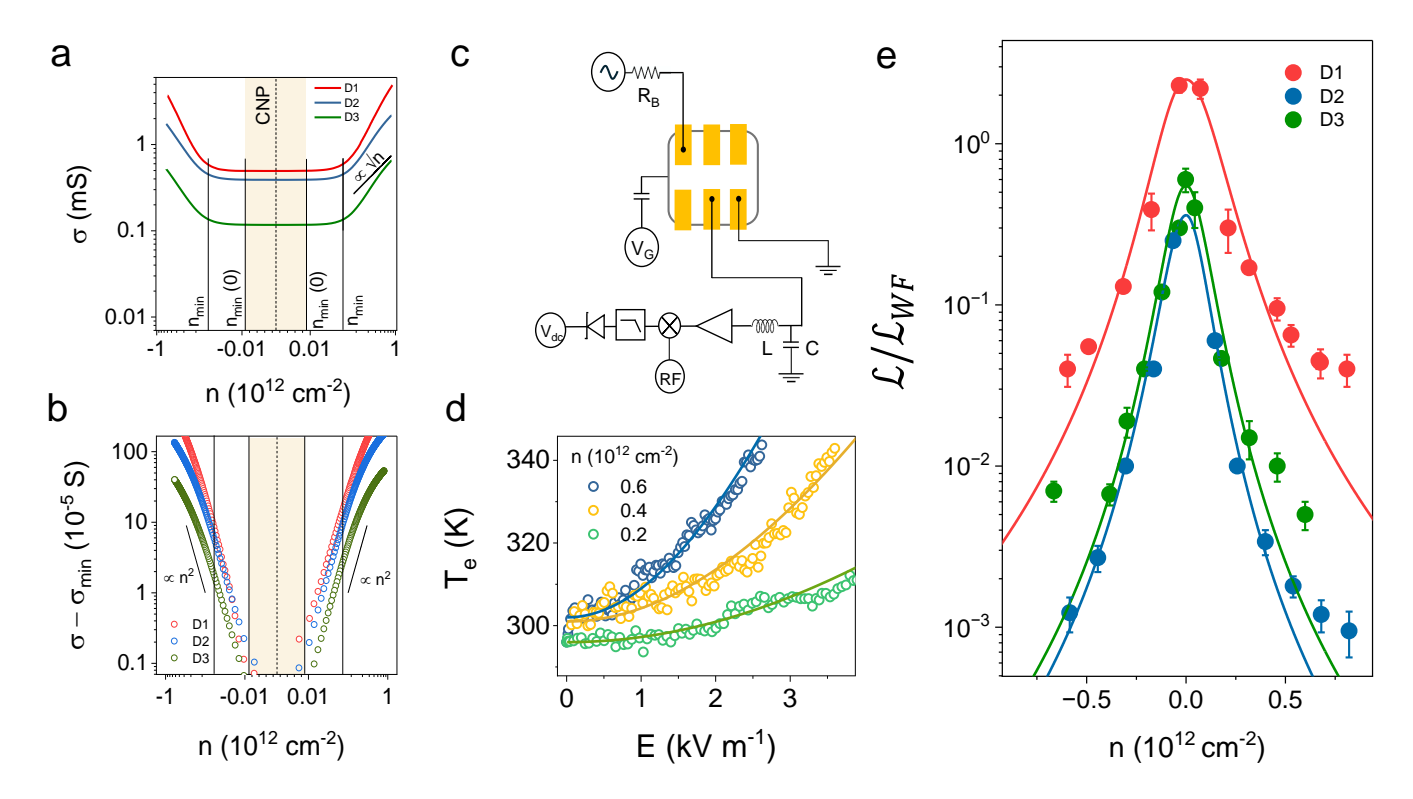


Figure 2. WF law violation as a signature of electron hydrodynamics: (a) Variation of σ as a function of n for three different devices D1, D2 and D3. The solid line (colored in black) indicates a \sqrt{n} dependence and serves as a guide to the eye. n_{\min} and $n_{\min}(0)$ have been indicated using vertical solid lines. The area shaded in light pink indicates $n < n_{\min}(0)$. (b) Variation of $\sigma - \sigma_{\min}$ as a function of n for three traces shown in (a). The solid line (colored in black) indicates a n^2 dependence and serves as a guide to the eye. The area shaded in light pink indicates $n < n_{\min}(0)$. (c) Schematic of the electrical circuit used for Johnson noise thermometry measurements. (d) Variation of T_e as a function of T_e for D2, at three different carrier concentrations given by $n(10^{12} \text{ cm}^{-2}) = 0.2, 0.4, 0.6$. (e) Variation of $\mathcal{L}/\mathcal{L}_{\text{WF}}$ as a function of n for three devices, D1, D2 and D3, all in pristine condition. The solid curves refer to the Lorentzian fit of the data, as per Eqn. 3. The error bars associated with the data points represent the standard deviation of results obtained from the experiment.

DEPENDENCE OF THE ELECTRICAL AND THERMAL CONDUCTIVITY ON DISORDER

We first explore the nature of charge and heat transport in the pristine hBN/Gr/hBN FETs, prior to the irradiation with UV. In all the measured devices, σ as a function of n at 300 K, shown in Fig. 2a, has similar features - (a) $n \leq n_{\min}(0)$: the inhomogeneous or disordered regime, where $\sigma = \sigma_{\min}$. (b) $n_{\min}(0) \leq n \leq n_{\min}$: the thermal regime, where thermally excited electrons and holes govern the number of carriers dictating σ . In Fig. 2b, we show the *n*-dependence of $\sigma - \sigma_{\min}$, where the thermal regime is characterised by $\sigma - \sigma_{\rm min} \propto n^2$, expected for the quantum critical hydrodynamic transport where the momentum-conserving scattering dominates the relaxation of current [15, 50]. (c) $n \ge n_{\min}$: the Fermi liquid regime where σ is controlled by free carriers generated by the gate voltage $V_{\rm G}$. Though the channel tends towards ballisticity, with $\sigma \propto \sqrt{n}$ at high densities, there is a small window at the intermediate carrier densities where $\sigma - \sigma_{\min} \propto n^2$, suggestive of a mono-component viscous fluid. In this regime, at low temperatures, we also observe quadratic dependence of σ on W (width of the channel) and negative local resistance, further establishing the viscous nature of electron transport [15]. These characteristics, however, usually get suppressed at temperatures as high as 300 K.

We subsequently measured the electronic thermal conductivity in these high-quality graphene devices with Johnson noise thermometry [13, 15], a well-established primary thermometry technique for accurate estimation of the electronic temperature $(T_{\rm e})$ in graphene. The schematic of the noise thermometry circuit is shown in Fig. 2c (See Supplementary Section S7 for details). At certain values of $V_{\rm G}$, we have performed Joule heating across the electronic channel by applying an in-plane DC electric field (E) and measured $T_{\rm e}$ as a function of E (Fig. 2c). Solving the heat diffusion equation [15] for this geometry, we get

$$T_{\rm e} = \frac{2\mathcal{L}}{3L^2E^2} \left[\left(T_{\rm c}^2 + \frac{L^2}{\mathcal{L}} E^2 \right)^{3/2} - \left(T_{\rm c}^2 \right)^{3/2} \right]$$
 (2)

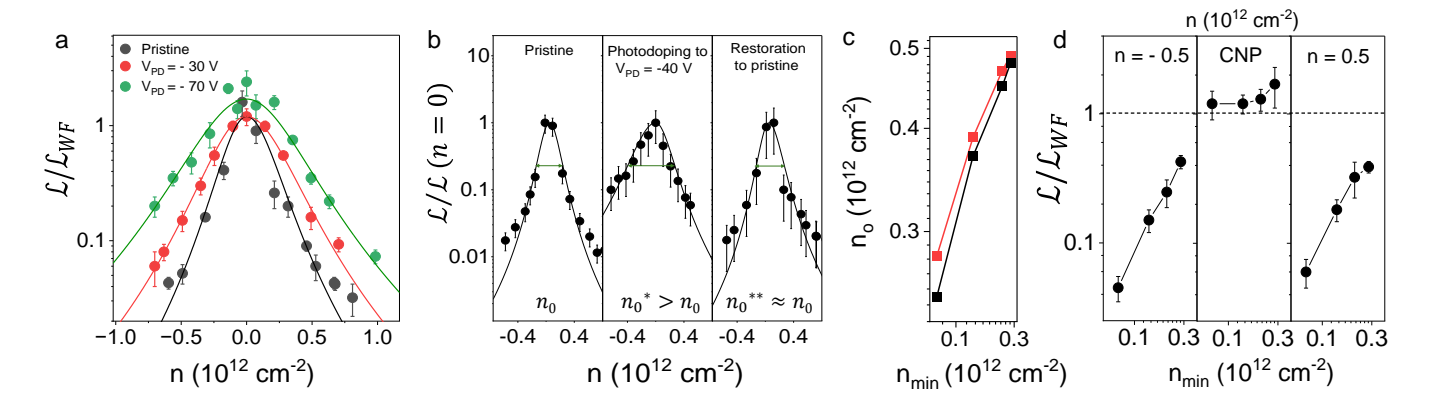


Figure 3. Signature of dynamically-tunable electron hydrodynamics in thermal transport: (a) Variation of $\mathcal{L}/\mathcal{L}_{WF}$ as a function of n for device D3 at different values of V_{PD} . The solid curves refer to the Lorentzian fits of the data, as per Eqn. 3. The error bars associated with the data points represent the standard deviation of results obtained from the experiment. (b) $\mathcal{L}/\mathcal{L}(n=0)$, where $\mathcal{L}(n=0)$ refers to the value of \mathcal{L} at the CNP, as a function of n for three different scenarios: (Left) Pristine graphene, (Center) After the pristine graphene has been UV-irradiated with $V_{PD} = -40$ V, (Right) After the UV-irradiated graphene is again subjected to UV radiation with $V_{PD} = 0$ V, thereby restoring the pristine conditions. The FWHMs (n_0, n_0^*, n_0^{**}) of the Lorentzian fits and the comparison of their magnitudes are mentioned near the bottom of each panel. The error bars presented here indicate the standard deviation of the experimental data points. (c) Variation of n_0 as a function of n_{\min} for device D3. (d) Variation of $\mathcal{L}/\mathcal{L}_{WF}$ as a function of n_{\min} for device D3, part of which has been shown in (a). The three panels refer to three distinct carrier density regimes: hole-doped (Left), CNP (Center) and electron-doped (Right). The dashed line refers to $\mathcal{L}/\mathcal{L}_{WF} = 1$. The error bars presented reflect the standard deviation of the experimental data points.

where L, \mathcal{L} and $T_{\rm c}$ are respectively the length of the channel, effective Lorentz number and electron temperature at the metallic contact. By fitting $T_{\rm e}$ against E using Eqn. 2, we estimate the \mathcal{L} at different densities for the electron fluid in graphene. The plot of $\mathcal{L}/\mathcal{L}_{\rm WF}$ as a function of n for three different devices (Fig. 2e) is reproducible across all our high-quality samples in pristine condition and exhibits a strong violation of WF law. Since the charge and heat flow pathways are decoupled in the presence of strong momentum-conserving scattering, this violation is considered to be a signature of viscous electronic flow [13, 51]. As per relativistic hydrodynamics, for a fluid of Dirac fermions [11, 52], $\mathcal{L}/\mathcal{L}_{\rm WF}$ varies

$$\mathcal{L}(n,T) = \frac{1}{e^2} \left[\frac{s(T)n_0(T)}{n^2 + n_0^2(T)} \right]^2$$
 (3)

where entropy density s(T) quantifies the thermal disorder of the Dirac fluid and $n_0(T)$ refers to an effective density scale, which determines the intrinsic conductivity of the electron fluid [11, 15, 53]. We observe a very good agreement between the experimental data and Eqn. 3, suggesting Dirac fluid-like electron flow in all three graphene FETs (Fig. 2e) near the CNP. Notably, although $\mathcal{L}/\mathcal{L}_{\text{WF}}$ tends to increase above that expected for a Dirac fluid (Eqn. 3) at high values of n, we do not observe any upturn that may suggest the restoration of Fermi-liquid like behaviour. Nonetheless, the thermal entropy density $s = en_0\sqrt{\mathcal{L}(n=0)}$ obtained from experimental values of n_0 and $\mathcal{L}(n=0)$ (\mathcal{L} at the CNP)

for the pristine graphene at 300 K agree with theoretical estimates [50, 54] within a factor of 2.

We next examine the n-dependence of $\mathcal{L}/\mathcal{L}_{WF}$ (during the reverse sweep cycle of $V_{\rm G}$ - see Supplementary Section S8) for different values of $V_{\rm PD}$, i.e. at different levels of disorder. Remarkably, $\mathcal{L}/\mathcal{L}_{\mathrm{WF}}$ continues to follow Eqn. 3 across all values of $V_{\rm PD}$ (Fig. 3a), although the width of the Lorentzian profile in n, characterised by n_0 , increases with increasing $V_{\rm PD}$. Since $\mathcal{L}/\mathcal{L}_{\rm WF} \approx 1$ near $n \approx 0$, this broadening reflects a progressive restoration of the Wiedemann-Franz (WF) law as disorder in the graphene channel increases. Importantly, this transition from a regime that violates the WF law to one that adheres to it is reversible. By reducing the disorder through UV irradiation - applied after setting $V_{\rm PD}=0$ V - we concurrently measure the electronic thermal conductivity across the channel. The results, shown in Fig. 3b, reveal that the FWHM of the Lorentzian n-dependence of $\mathcal{L}/\mathcal{L}_{WF}$ initially increases from n_0 to n_0^* $(n_0^* > n_0)$ as $V_{\rm PD}$ is swept from 0 to -40 V, and subsequently returns to approximately n_0 as $V_{\rm PD}$ is brought back from -40 to 0 V. This reversibility highlights the potential for dynamically tuning a hydrodynamic transport regime within a disordered graphene monolayer.

Further, this establishes n_0 as a crucial parameter that can be used to quantify the impact of disorder on the thermal transport in the graphene channel. With increasing n_{\min} , n_0 is found to increase monotonically, as shown in Fig. 3c. The nature of this variation is theoretically expected to depend on the nature of electron-impurity scattering [55]; however, a quantitative understanding of

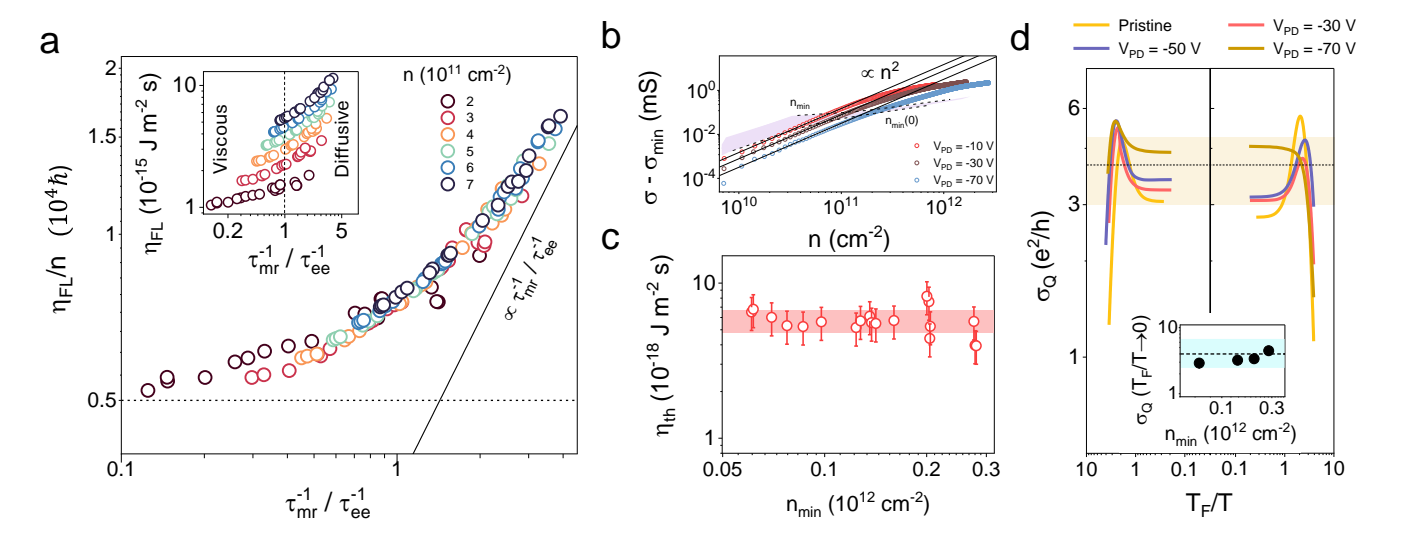


Figure 4. Effect of disorder on shear viscosity in the Fermi liquid and thermal regimes: (a) $\eta_{\rm FL}/n$ as a function of $\tau_{\rm mr}^{-1}/\tau_{\rm ee}^{-1}$ for different carrier densities, indicated using symbols of different color. The horizontal dashed line points towards the asymptotic tendency of $\eta_{\rm FL}/n$. In the diffusive limit, the solid line indicates $\eta_{\rm FL}/n \propto \tau_{\rm mr}^{-1}/\tau_{\rm ee}^{-1}$ and serves as a guide to the eye. [Inset] $\eta_{\rm FL}$ as a function of $\tau_{\rm mr}^{-1}/\tau_{\rm ee}^{-1}$ for different carrier densities. The vertical dotted line indicated by $\tau_{\rm mr}^{-1}/\tau_{\rm ee}^{-1} = 1$ highlights the hydrodynamic-to-diffusive crossover. (b) The plot of $\sigma - \sigma_{\rm min}$ as a function of n for three different values of $V_{\rm PD}$ in device D3. The solid lines scale as n^2 and serve as guides to the eye. The two dashed lines denote $n_{\rm min}$ and $n_{\rm min}(0)$, with the enclosed region indicating the thermal regime being colored in blue. (c) Shear viscosity in the thermal regime ($\eta_{\rm th}$) as a function of $n_{\rm min}$ in device D3. The colored region highlights the range of variation of $\eta_{\rm th}$. The error bars presented here indicate the standard deviation of the variable. (d) $\sigma_{\rm Q}$ as a function of $T_{\rm F}/T$ for device D3 at different values of $V_{\rm PD}$. (Inset) $\sigma_{\rm Q}$ for $T_{\rm F}/T \to 0$ as a function of $n_{\rm min}$, with a colored region indicating the range of variation of the data points. The unit along y-axis is e^2/h . The dashed horizontal line corresponds to $4e^2/h$.

this dependence is still lacking.

The key feature of the data shown in Fig. 3a is a clear increasing trend in $\mathcal{L}/\mathcal{L}_{\mathrm{WF}}$ with n_{min} at high electron and hole densities, as demonstrated in Fig. 3d. This is consistent with the expectation that the introduction of electronic disorder boosts momentum relaxing scattering [53, 55], leading to the increase of $\mathcal{L}/\mathcal{L}_{\mathrm{WF}}$ towards ≈ 1 - paving the way for a disorder-enabled hydrodynamic regime. Further, experimental data demonstrates a negligible variation in $\mathcal{L}/\mathcal{L}_{\mathrm{WF}}$ near the CNP at $T \simeq 300~\mathrm{K}$ (Fig. 3d). This can be attributed to the suppression of WF law violation near the Dirac point at room temperature by electron-phonon scattering and the presence of disorder in the system leads to a minor increase in $\mathcal{L}/\mathcal{L}_{\mathrm{WF}}$ at very high n_{min} , which can be explained within the conventional Fermi liquid framework [56, 57].

DISCUSSION

Our experimental strategy to dynamically tune the momentum-relaxing scattering in the same device allows us to explore some of the key features in viscous transport as a function of disorder in a quantitative manner. An important parameter is the shear viscosity (η) , which varies differently as a function of carrier density in the thermal regime $(\eta = \eta_{\rm th})$ and in the Fermi liquid regime

 $(\eta = \eta_{\rm FL}).$

We first focus on the Fermi liquid regime given by $n \gtrsim 10^{11}~{\rm cm^{-2}}$ and $l_{\rm ee} \ll W$, where $T_{\rm F} > T$, and $\eta_{\rm FL} = n^2 e^2 W^2/12\sigma$ [58, 59] represents the viscous friction among the constituent particles of a monocomponent charged fluid, composed of either electrons or holes. In Fig. 4a (inset), $\eta_{\rm FL}$ has been plotted as a function of $\tau_{\rm mr}^{-1}/\tau_{\rm ee}^{-1}$ at different carrier densities. With increasing disorder, $\eta_{\rm FL}$ varies weakly in the viscous limit and starts increasing monotonically for $\tau_{\rm mr}^{-1} > \tau_{\rm ee}^{-1}$ across the experimental range $(1-7\times10^{11}~{\rm cm^{-2}})$ of n. Although $\eta_{\rm FL}$ in a disordered system has never been precisely defined, previous works [60, 61] have predicted electron-impurity scattering to enhance viscous effects. In the presence of charged impurity scattering $(\tau_{\rm mr}^{-1} \propto \sqrt{n})$, and noting that $\eta_{\rm FL} = nm\nu$ where $m = \hbar k_{\rm F}/v_{\rm F}$ and $\nu = \frac{1}{4}v_{\rm F}^2\tau_{\rm ee}$ are, respectively, the effective mass and kinematic viscosity, we find,

$$\frac{\eta_{\rm FL}}{n} = \frac{\hbar^3 v_{\rm F}^2}{n_{\rm d} V_0^2} \frac{\tau_{\rm mr}^{-1}}{\tau_{\rm ee}^{-1}} \tag{4}$$

where the electron-impurity scattering rate is given by $\tau_{\rm mr}^{-1} = \left(\frac{n_{\rm d}V_0^2\sqrt{\pi}}{4\hbar^2v_{\rm F}}\right)\sqrt{n}$ [47], $n_{\rm d}$ being the short-ranged neutral impurity concentration and V_0 being the strength of the impurity scattering potential.

For $n \gtrsim 10^{11}~\rm cm^{-2}$, we observe that $\eta_{\rm FL}/n$ collapses onto a universal behaviour when plotted against $\tau_{\rm mr}^{-1}/\tau_{\rm ee}^{-1}$, exhibiting a linear increase at large values, in excellent agreement with Eqn. 4 for both electrons (Fig. 4a) and holes (See Supplementary Section S9). The slope of the data for $\tau_{\rm mr}^{-1}/\tau_{\rm ee}^{-1}\gg 1$ reveals the impurity scattering potential V_0 to be $\approx 0.03~\rm eV~nm^{-2}$, which is very close to theoretical estimates [62]. The physical mechanism underlying this linear increase is, however, not well understood.

On the other hand. as the system approaches the clean limit $(\tau_{\rm mr}^{-1}/\tau_{\rm ee}^{-1}\ll 1)$, the shear viscosity of the graphene channel is given by $\eta_{\rm FL}=nm\nu=\hbar\sqrt{\pi}n^{3/2}(\nu/v_{\rm F})$. Now, for the pristine graphene channel, $\nu\propto 1/\sqrt{n}$ (See Supplementary Section S10), which is comparable to the decreasing trend of ν on n observed in previous experimental results [9, 63]. Finally, we observe in Fig. 4a, that the shear viscosity per unit carrier, indicated by $\eta_{\rm FL}/n$, exhibits an asymptotic saturation to $\approx 5000\hbar$, as theoretically expected from a clean Fermi liquid [54, 64].

Close to the Dirac point, electrons and holes collide with each other at the Planckian rate [65], which is given by $\tau_{\rm P}^{-1} = \alpha^2 k_{\rm B} T/\hbar$ and is solely determined by the temperature T of the electronic system. The shear viscosity of these thermally excited electrons and holes is evaluated using the expression $\eta_{\rm th} = e^2 v_{\rm F} l_{mr} \tau_{\rm P}/2A_{\rm th}(T)$, where $A_{\rm th}(T)$ is the coefficient of n^2 in the n-dependence of σ [15, 57].

In the thermal regime, the fluidic nature of electronic motion results in a n^2 dependence of the electrical conductivity σ , as shown in Fig. 4b. However, the addition of disorder to ultra-clean graphene barely affects $\eta_{\rm th}$, as seen in Fig. 4c. With increasing $n_{\rm min}$, the thermal shear viscosity stays constant at $\eta_{\rm th} \simeq 6 \times 10^{-18}$ J m⁻² s. This can be explained on the basis of the origin of this viscous motion, caused entirely by the thermally excited electrons and holes $(n_{\rm th})$ near the CNP. As a result, when disorder is incorporated into the system, it changes $n_{\rm min}(0)$ and thus $n_{\rm min}$, but $n_{\rm th}$ remains constant, thereby forcing $\eta_{\rm th}$ to remain constant as well.

The inability of UV-activated disorder to affect the thermal properties of the ultra-clean graphene near the Dirac point suggests that the quantum critical behaviour of graphene in this regime remains robust against the disorder created by the radiation. This is confirmed in the plot of $\sigma_{\rm Q}$, evaluated using $\sigma_{\rm Q} = \kappa_{\rm e} \sigma/v_{\rm F} l_{\rm mr} s_{\rm th}$ [15, 57] with $s_{\rm th}$ being the thermal entropy density [11, 50, 54], as a function of $T_{\rm F}/T$ (Fig. 4d) We clearly see the saturation of $\sigma_{\rm Q}$, close to $T_{\rm F}/T \to 0$ for different disorder densities, near a universal constant with the magnitude varying around $(4 \pm 1) \ e^2/h$ (inset of Fig. 4d), in agreement with theoretical expectations [15, 50].

In conclusion, our experimental results have successfully established a non-invasive tool, comprising a combination of UV radiation and gate electric field, which is capable of reversibly tuning the disorder level in a high-

quality hBN-encapsulated graphene monolayer with high precision. This control over the introduction of disorder in a clean graphene FET facilitates the demonstration of a dynamically tunable charged fluid, which was confirmed by thermal noise spectroscopy of the disordered Dirac fermions navigating through the UV-irradiated graphene layer. Additionally, our results assess the impact of charged disorder on electronic viscosity in monolayer graphene, offering new insights into both the Dirac and Fermi liquid phases. Our findings act as the testing bed for several existing theoretical models of relativistic hydrodynamics, focusing on the interplay of momentum-conserving and momentum-relaxing scattering to explain the onset of electron fluidity in monolayer graphene.

ACKNOWLEDGMENT

The authors gratefully acknowledge the usage of the MNCF and NNFC facilities at CeNSE, IISc. The authors would also like to acknowledge fruitful discussions with N. Chaddha and S. Mukerjee. A.G. acknowledges financial support from J. C. Bose Fellowship and a project under NanoMission, Department of Science and Technology, India. Ak.G. thanks the Ministry of Education, Govt. of India, for the Prime Minister's Research Fellowship (PMRF). K.W. and T.T. acknowledge support from the JSPS KAKENHI (Grant Numbers 21H05233 and 23H02052), the CREST (JPMJCR24A5), JST and World Premier International Research Center Initiative (WPI), MEXT, Japan.

- * equal contribution; akashgugnani@iisc.ac.in
- † equal contribution; aniketm@iisc.ac.in
- [‡] arindam@iisc.ac.in
- C. R. Dean, A. F. Young, I. Meric, C. Lee, L. Wang, S. Sorgenfrei, K. Watanabe, T. Taniguchi, P. Kim, K. L. Shepard, et al., Boron nitride substrates for high-quality graphene electronics, Nat. Nanotechnol. 5, 722 (2010).
- [2] L. Lin, J. Zhang, H. Su, J. Li, L. Sun, Z. Wang, F. Xu, C. Liu, S. Lopatin, Y. Zhu, et al., Towards super-clean graphene, Nat. Commun. 10, 1912 (2019).
- [3] Q. H. Wang, K. Kalantar-Zadeh, A. Kis, J. N. Coleman, and M. S. Strano, Electronics and optoelectronics of twodimensional transition metal dichalcogenides, Nat. Nanotechnol. 7, 699 (2012).
- [4] Y. Wang and M. Chhowalla, Making clean electrical contacts on 2D transition metal dichalcogenides, Nat. Rev. Phys. 4, 101 (2022).
- [5] P. Gallagher, C.-S. Yang, T. Lyu, F. Tian, R. Kou, H. Zhang, K. Watanabe, T. Taniguchi, and F. Wang, Quantum-critical conductivity of the Dirac fluid in graphene, Science 364, 158 (2019).
- [6] M. J. Ku, T. X. Zhou, Q. Li, Y. J. Shin, J. K. Shi, C. Burch, L. E. Anderson, A. T. Pierce, Y. Xie, A. Hamo,

- et al., Imaging viscous flow of the Dirac fluid in graphene, Nature **583**, 537 (2020).
- [7] U. Vool, A. Hamo, G. Varnavides, Y. Wang, T. X. Zhou, N. Kumar, Y. Dovzhenko, Z. Qiu, C. A. Garcia, A. T. Pierce, et al., Imaging phonon-mediated hydrodynamic flow in WTe₂, Nat. Phys. 17, 1216 (2021).
- [8] J. A. Sulpizio, L. Ella, A. Rozen, J. Birkbeck, D. J. Perello, D. Dutta, M. Ben-Shalom, T. Taniguchi, K. Watanabe, T. Holder, et al., Visualizing Poiseuille flow of hydrodynamic electrons, Nature 576, 75 (2019).
- [9] D. Bandurin, I. Torre, R. K. Kumar, M. Ben Shalom, A. Tomadin, A. Principi, G. Auton, E. Khestanova, K. Novoselov, I. Grigorieva, et al., Negative local resistance caused by viscous electron backflow in graphene, Science 351, 1055 (2016).
- [10] A. Block, A. Principi, N. C. Hesp, A. W. Cummings, M. Liebel, K. Watanabe, T. Taniguchi, S. Roche, F. H. Koppens, N. F. van Hulst, et al., Observation of giant and tunable thermal diffusivity of a Dirac fluid at room temperature, Nat. Nanotechnol. 16, 1195 (2021).
- [11] S. Li, A. Andreev, and A. Levchenko, Hydrodynamic electron transport in graphene Hall-bar devices, Phys. Rev. B 105, 155307 (2022).
- [12] A. I. Berdyugin, S. Xu, F. Pellegrino, R. Krishna Kumar, A. Principi, I. Torre, M. Ben Shalom, T. Taniguchi, K. Watanabe, I. Grigorieva, et al., Measuring Hall viscosity of graphene's electron fluid, Science 364, 162 (2019).
- [13] J. Crossno, J. K. Shi, K. Wang, X. Liu, A. Harzheim, A. Lucas, S. Sachdev, P. Kim, T. Taniguchi, K. Watanabe, et al., Observation of the Dirac fluid and the breakdown of the Wiedemann-Franz law in graphene, Science 351, 1058 (2016).
- [14] M. L. Palm, C. Ding, W. S. Huxter, T. Taniguchi, K. Watanabe, and C. L. Degen, Observation of current whirlpools in graphene at room temperature, Science 384, 465 (2024).
- [15] A. Majumdar, N. Chadha, P. Pal, A. Gugnani, B. Ghawri, K. Watanabe, T. Taniguchi, S. Mukerjee, and A. Ghosh, Universality in quantum critical flow of charge and heat in ultra-clean graphene, Nat. Phys. (2025), [In Press]; preprint available at arXiv:2501.03193.
- [16] A. Aharon-Steinberg, T. Völkl, A. Kaplan, A. K. Pariari, I. Roy, T. Holder, Y. Wolf, A. Y. Meltzer, Y. Myasoedov, M. E. Huber, et al., Direct observation of vortices in an electron fluid, Nature 607, 74 (2022).
- [17] J. Estrada-Álvarez, F. Domínguez-Adame, and E. Díaz, Alternative routes to electron hydrodynamics, Commun. Phys. 7, 138 (2024).
- [18] Q. Hong, M. Davydova, P. J. Ledwith, and L. Levitov, Superscreening by a retroreflected hole backflow in tomographic electron fluids, Phys. Rev. B 109, 085126 (2024).
- [19] J. Hofmann and S. Das Sarma, Collective modes in interacting two-dimensional tomographic Fermi liquids, Phys. Rev. B 106, 205412 (2022).
- [20] Y. Zeng, H. Guo, O. M. Ghosh, K. Watanabe, T. Taniguchi, L. S. Levitov, and C. R. Dean, Quantitative measurement of viscosity in two-dimensional electron fluids, arXiv preprint arXiv:2407.05026 (2024).
- [21] L. Wang, I. Meric, P. Huang, Q. Gao, Y. Gao, H. Tran, T. Taniguchi, K. Watanabe, L. Campos, D. Muller, et al., One-dimensional electrical contact to a two-dimensional material, Science 342, 614 (2013).
- [22] W. Wang, X. Ma, Z. Dai, S. Zhang, Y. Hou, G. Wang, Q. Li, Z. Zhang, Y. Wei, and L. Liu, Mechanical behavior

- of blisters spontaneously formed by multilayer 2D materials, Adv. Mater. Int. 9, 2101939 (2022).
- [23] Y.-C. Lin, C. Jin, J.-C. Lee, S.-F. Jen, K. Suenaga, and P.-W. Chiu, Clean transfer of graphene for isolation and suspension, ACS Nano 5, 2362 (2011).
- [24] N. Xin, J. Lourembam, P. Kumaravadivel, A. Kazant-sev, Z. Wu, C. Mullan, J. Barrier, A. A. Geim, I. Grigorieva, A. Mishchenko, et al., Giant magnetoresistance of Dirac plasma in high-mobility graphene, Nature 616, 270 (2023).
- [25] Y. Nam, D.-K. Ki, D. Soler-Delgado, and A. F. Morpurgo, Electron-hole collision limited transport in charge-neutral bilayer graphene, Nat. Phys. 13, 1207 (2017).
- [26] L. Jin, S. E. Zeltmann, H. S. Choe, H. Liu, F. I. Allen, A. M. Minor, and J. Wu, Disorder recovers the Wiedemann-Franz law in the metallic phase of VO₂, Phys. Rev. B 102, 041120 (2020).
- [27] C. Neumann, L. Rizzi, S. Reichardt, B. Terrés, T. Khodkov, K. Watanabe, T. Taniguchi, B. Beschoten, and C. Stampfer, Spatial control of Laser-Induced Doping Profiles in Graphene on Hexagonal Boron Nitride, ACS Appl. Mater. & Int. 8, 9377 (2016).
- [28] L. Ju, J. Velasco, E. Huang, S. Kahn, C. Nosiglia, H.-Z. Tsai, W. Yang, T. Taniguchi, K. Watanabe, Y. Zhang, et al., Photoinduced doping in heterostructures of graphene and boron nitride, Nat. Nanotechnol. 9, 348 (2014).
- [29] Z. Luo, N. J. Pinto, Y. Davila, and A. Charlie Johnson, Controlled doping of graphene using ultraviolet irradiation, Appl. Phys. Lett. 100 (2012).
- [30] K. Roy, M. Padmanabhan, S. Goswami, T. P. Sai, G. Ramalingam, S. Raghavan, and A. Ghosh, Graphene– MoS₂ hybrid structures for multifunctional photoresponsive memory devices, Nat. Nanotechnol. 8, 826 (2013).
- [31] E. Quezada-Lopez, F. Joucken, H. Chen, A. Lara, J. Davenport, K. Hellier, T. Taniguchi, K. Watanabe, S. Carter, A. Ramirez, et al., Persistent and reversible electrostatic control of doping in graphene/hexagonal boron nitride heterostructures, Journ. of Appl. Phys. 127 (2020).
- [32] N. W. Ashcroft, N. D. Mermin, and S. Rodriguez, Solid state physics, American Journal of Physics 46, 116 (1978).
- [33] L. A. Ponomarenko, A. Principi, A. D. Niblett, W. Wang, R. V. Gorbachev, P. Kumaravadivel, A. I. Berdyugin, A. V. Ermakov, S. Slizovskiy, K. Watanabe, et al., Extreme electron-hole drag and negative mobility in the Dirac plasma of graphene, Nat. Commun. 15, 9869 (2024).
- [34] G. Cassabois, P. Valvin, and B. Gil, Hexagonal boron nitride is an indirect bandgap semiconductor, Nat. Photon. 10, 262 (2016).
- [35] T. Ahmed, S. Islam, T. Paul, N. Hariharan, S. Elizabeth, and A. Ghosh, A generic method to control hysteresis and memory effect in van der waals hybrids, Mater. Res. Express 7, 014004 (2020).
- [36] M. Uddin, J. Li, J. Lin, and H. Jiang, Probing carbon impurities in hexagonal boron nitride epilayers, Appl. Phys. Lett. 110 (2017).
- [37] X. Du, J. Li, J. Lin, and H. Jiang, The origin of deep-level impurity transitions in hexagonal boron nitride, Appl. Phys. Lett. 106 (2015).
- [38] X. Du, J. Li, J. Lin, and H. Jiang, The origins of near band-edge transitions in hexagonal boron nitride epilay-

- ers, Appl. Phys. Lett. 108 (2016).
- [39] A. Gao, E. Zoethout, J. M. Sturm, C. J. Lee, and F. Bijkerk, Defect formation in single layer graphene under extreme ultraviolet irradiation, Appl. Surf. Sci. 317, 745 (2014).
- [40] H.-Y. Xie and M. S. Foster, Transport coefficients of graphene: Interplay of impurity scattering, Coulomb interaction, and optical phonons, Phys. Rev. B 93, 195103 (2016).
- [41] F. Ghahari, H.-Y. Xie, T. Taniguchi, K. Watanabe, M. S. Foster, and P. Kim, Enhanced thermoelectric power in graphene: Violation of the Mott relation by inelastic scattering, Phys. Rev. Lett. 116, 136802 (2016).
- [42] K. Kaasbjerg, K. S. Thygesen, and K. W. Jacobsen, Unraveling the acoustic electron-phonon interaction in graphene, Phys. Rev. B — Cond. Matt. and Mat. Phys. 85, 165440 (2012).
- [43] V. Perebeinos and P. Avouris, Inelastic scattering and current saturation in graphene, Phys. Rev. B — Cond. Matt. and Mat. Phys. 81, 195442 (2010).
- [44] E. Hwang and S. Das Sarma, Acoustic phonon scattering limited carrier mobility in two-dimensional extrinsic graphene, Phys. Rev. B 77, 115449 (2008).
- [45] K. I. Bolotin, K. J. Sikes, J. Hone, H. Stormer, and P. Kim, Temperature-dependent transport in suspended graphene, Phys. Rev. Lett. 101, 096802 (2008).
- [46] D. K. Efetov and P. Kim, Controlling electron-phonon interactions in graphene at ultrahigh carrier densities, Phys. Rev. Lett. 105, 256805 (2010).
- [47] S. Das Sarma, S. Adam, E. H. Hwang, and E. Rossi, Electronic transport in two-dimensional graphene, Rev. Mod. Phys. 83, 407 (2011).
- [48] S. Sarkar, K. R. Amin, R. Modak, A. Singh, S. Mukerjee, and A. Bid, Role of different scattering mechanisms on the temperature dependence of transport in graphene, Sci. Rep. 5, 16772 (2015).
- [49] J. H. Gosling, O. Makarovsky, F. Wang, N. D. Cottam, M. T. Greenaway, A. Patanè, R. D. Wildman, C. J. Tuck, L. Turyanska, and T. M. Fromhold, Universal mobility characteristics of graphene originating from charge scattering by ionised impurities, Commun. Phys. 4, 30 (2021).
- [50] M. Müller, J. Schmalian, and L. Fritz, Graphene: A nearly perfect fluid, Phys. Rev. Lett. 103, 025301 (2009).
- [51] A. Principi and G. Vignale, Violation of the Wiedemann– Franz law in Hydrodynamic Electron Liquids, Phys. Rev. Lett. 115, 056603 (2015).
- [52] A. Lucas and K. C. Fong, Hydrodynamics of electrons in graphene, Journ. of Phys.: Cond. Matt. **30**, 053001

- (2018).
- [53] S. Li, A. Levchenko, and A. Andreev, Hydrodynamic electron transport near charge neutrality, Phys. Rev. B 102, 075305 (2020).
- [54] I. Yudhistira, R. Afrose, and S. Adam, Nonmonotonic temperature dependence of electron viscosity and crossover to high-temperature universal viscous fluid in monolayer and bilayer graphene, Phys. Rev. B 111, 085433 (2025).
- [55] M. Zarenia, A. Principi, and G. Vignale, Disorderenabled hydrodynamics of charge and heat transport in monolayer graphene, 2D Mater. 6, 035024 (2019).
- [56] Y.-T. Tu and S. Das Sarma, Wiedemann-Franz law in graphene, Phys. Rev. B 107, 085401 (2023).
- [57] A. Lucas, J. Crossno, K. C. Fong, P. Kim, and S. Sachdev, Transport in inhomogeneous quantum critical fluids and in the Dirac fluid in graphene, Phys. Rev. B 93, 075426 (2016).
- [58] H. Guo, E. Ilseven, G. Falkovich, and L. S. Levitov, Higher-than-ballistic conduction of viscous electron flows, PNAS 114, 3068 (2017).
- [59] R. Krishna Kumar, D. Bandurin, F. Pellegrino, Y. Cao, A. Principi, H. Guo, G. Auton, M. Ben Shalom, L. Ponomarenko, G. Falkovich, et al., Superballistic flow of viscous electron fluid through graphene constrictions, Nat. Phys. 13, 1182 (2017).
- [60] W. Chen and W. Zhu, Viscosity of disordered Dirac electrons, Phys. Rev. B 106, 014205 (2022).
- [61] I. S. Burmistrov, M. Goldstein, M. Kot, V. D. Kurilovich, and P. D. Kurilovich, Dissipative and Hall viscosity of a disordered 2D electron gas, Phys. Rev. Lett. 123, 026804 (2019).
- [62] M. Davoudiniya, B. Yang, and B. Sanyal, Influence of ab initio derived site-dependent hopping parameters on electronic transport in graphene nanoribbons, Phys. Chem. Chem. Phys. 26, 1936 (2024).
- [63] A. Talanov, J. Waissman, A. Hui, B. Skinner, K. Watanabe, T. Taniguchi, and P. Kim, Observation of electronic viscous dissipation in graphene magneto-thermal transport, arXiv preprint arXiv:2406.13799 (2024).
- [64] A. Principi, G. Vignale, M. Carrega, and M. Polini, Bulk and shear viscosities of the two-dimensional electron liquid in a doped graphene sheet, Phys. Rev. B 93, 125410 (2016).
- [65] J. A. N. Bruin, H. Sakai, R. S. Perry, and A. Mackenzie, Similarity of scattering rates in metals showing T-linear resistivity, Science 339, 804 (2013).